



DEPARTMENT OF
PHYSICS

PEDRO DAVID ARSÉNIO COPETO

BSc in Physics Engineering

LIGHT FRAGMENT DETECTION USING RESISTIVE PLATE CHAMBERS

CONTRIBUTION TO GSI EXPERIMENT G249

MASTER IN PHYSICS ENGINEERING

NOVA University Lisbon

Draft: June 17, 2025

LIGHT FRAGMENT DETECTION USING RESISTIVE PLATE CHAMBERS

CONTRIBUTION TO GSI EXPERIMENT G249

PEDRO DAVID ARSÉNIO COPETO

BSc in Physics Engineering

Adviser: Daniel Galaviz Redondo

Assistant Professor, University of Lisbon

Co-advisers: João Duarte Neves Cruz

Associate Professor, NOVA University Lisbon

John Doe other Co-Adviser Name

Full Professor, NOVA University Lisbon

ABSTRACT

This will be my abstract.

Keywords: Resistive plate chamber, Quasi-free scattering, Gaseous detectors, One keyword more, The last keyword

RESUMO

Este vai ser o meu resumo.

Palavras-chave: Câmara de placas resistivas, Dispersão quase livre, Detetores gasosos, A última palavra-chave

CONTENTS

List of Figures	v
Acronyms	vii
1 Introduction	1
1.1 Introduction	1
1.1.1 The Liquid-drop Model	2
1.1.2 The Shell Model	2
1.1.3 Conclusion	4
1.2 The FAIR Facility	4
1.3 Author's Contribution and Thesis Overview	6
2 Direct Reactions as Spectroscopic Tools	7
2.1 Introduction	7
2.2 Transfer Reactions	7
2.3 Knockout Reactions	8
2.4 From Knockout to Quasi-Free Scattering	8
2.5 Quasi-free Scattering Reactions	9
2.5.1 Introduction to Quasi-Free Scattering	9
2.5.2 Historical Context and the Electron-Induced Paradigm	9
2.5.3 Proton-Induced QFS and DWIA Evolution	10
2.5.4 The Modern Era: Inverse Kinematics and Exotic Nuclei	10
2.5.5 Benchmark and Current Frontiers	11
3 Experiment	12
3.1 Context and Goal of the Experiment	12
3.2 The GSI Accelerator System	13
3.2.1 From Source to Experimental Cave	13
3.2.2 Beam used in Experiment	17
3.3 R ³ B Setup	18

3.3.1	Role of each detector	21
3.3.2	Particular Role of RPC	23
3.3.3	Main DAQ	23
3.4	Personal Contribution to the Experiment	24
4	RPC	25
4.1	History of RPCs/ Introduction	25
4.2	Properties	25
4.3	Build (components, electronics, gas mixture, DAQ, etc.)	25
4.3.1	RPC Build	26
4.3.2	RPC Electronics	27
4.3.3	RPC Gas Mixture	27
4.4	Previous Experiments and Results	29
4.5	Preparation for an Experiment	30
4.6	Calibration	30
5	Simulation Framework	31
5.1	Geant4	31
5.2	ROOT	32
5.3	R3BRoot	32
5.4	Plots	33
5.5	Multidimensional Fitting	33
5.5.1	Application to the RPC and FOOT Detectors	33
5.5.2	Validation of the MDF Models	34
5.6	Conclusions for the Experiment	34
6	Results	35
	Bibliography	36
	Appendices	
A	RPC Plots	42
	Annexes	
I	GSI Accelerator Facility	43

LIST OF FIGURES

1.1	Single-particle shell model level scheme illustrating the origin of nuclear magic numbers after incorporating spin-orbit coupling. The diagram shows the energy splitting of nuclear orbitals due to spin-orbit interaction, leading to the observed magic numbers (circled) corresponding to closed shells at nucleon numbers 2, 8, 20, 28, 50, 82, 126, and 184. The levels are labeled with their orbital and total angular momentum quantum numbers nlj , and the associated degeneracy $(2j+1)$ is indicated on the right. Reprinted figure from Ref. [9]	3
1.2	Layout of GSI-FAIR with the existing and planned beamlines shown in blue and red, respectively. The experimental sites are marked in black (figure: GSI Darmstadt). © Copyright: GSI/FAIR.	5
2.1	Schematic diagram of a QFS reaction induced by a proton p^+ on a nucleus A via elastic scattering off the virtual constituent particle X^* . Three real particles are generated in the final state: the scattered proton p^+ , the knock-out cluster X and the spectator nuclear fragment $(A-X^*)$. Reprinted figure from Ref. [24]	10
3.1	Schematic layout of the GSI Helmholtzzentrum accelerator facility. The diagram shows the major components including the ion sources, the UNILAC linear accelerator, the SIS18 synchrotron, the Fragment Separator (FRS), and the associated experimental halls [36].	13
3.2	Detailed schematic of the UNILAC accelerator. The figure highlights the beamline structure from ion sources through the High Current Injector (HSI), Radio-Frequency Quadrupole (RFQ), Interdigital H-mode Drift Tube Linacs (IH-DTL), gas stripper section, Alvarez Drift Tube Linac (DTL), and the transfer line to SIS18. Beam diagnostic and stripping sections are also labeled [39].	14
3.3	Plan view of the SIS18 heavy-ion synchrotron, illustrating its 12 identical lattice sections, dipole and quadrupole magnet configurations, RF acceleration cavities, and positions of beam diagnostic systems [41].	15

3.4	Schematic of the FRS system showing its dipole magnet sections, dispersive and achromatic focal planes (F1–F8), and the separation of rare isotope beams. The figure also shows the branching to dedicated experimental areas, including the Direct Branch, Ring Branch (ESR), and the experimental caves [43]. . . .	16
3.5	Layout of GSI-FAIR with Cave C highlighted, where the prototype of the future NUSTAR R ³ B setup stands and where the present experiment took place. .	16
3.6	Expected secondary cocktail beam of ²⁵ F in Cave C as obtained by LISE++ calculations. The numbers under the names of isotopes indicate calculated rates per second. Reprinted figure from Ref. [31].	17
3.7	Sketch of the experimental setup at R ³ B.	18
3.8	Simulated trajectories through the GLAD magnet. The color map indicates the magnetic field of the magnet. The LH2 target is located at the (0,0,0) point in front of GLAD. Reprinted figure from Ref. [31].	19
3.9	20
3.10	Schematic representation of the R ³ B setup with beam lines.	21
4.1	Schematic representation of the top view of the RPC.	26
4.2	RPC Strip Efficiency	30
5.1	Example of an event in a simulation. In this case, there's a ¹⁴ C passing through ToFD, a Deuteron passing through the RPC and 3 neutrons going to NeuLAND.	32

ACRONYMS

CALIFA	CALorimeter for In-Flight detection of gamma-rays and charged pArticles (p. 21)
DAQ	Data Acquisition (pp. 23, 25)
FAIR	Facility for Antiproton and Ion Research (pp. 4–6, 15, 16)
FRS	FRagment Separator (pp. 15, 17)
GLAD	GSI Large Acceptance Dipole (p. 21)
NeuLAND	New Large-Area Neutron Detector (p. 21)
QFS	Quasi-free Scattering (pp. 9–12)
R³B	Reactions with Relativistic Radioactive Beams (pp. 6, 12, 13, 15, 18, 21, 27, 29, 31–34)
RPC	Resistive Plate Chamber (pp. 21, 26, 32–34)
ToFD	Time-of-Flight Detector (p. 21)

INTRODUCTION

"The important thing in science is not so much to obtain new facts as to discover new ways of thinking about them."

Sir William Lawrence Bragg

1.1 Introduction

Since the birth of Nuclear Physics, with the discovery of the atomic nucleus by Ernest Rutherford in 1911 [1], this area has proved to be a fascinating field for scientific research displaying a rich variety of quantum phenomena. Many features of the nucleons in the nucleus exhibited are similar to the structure and behavior of atomic electrons in the atom. Similar descriptions for energy levels and shells, spins and angular momentum have emerged.

But there are some differences:

1. The dominating force inside the nucleus is the strong force rather than the electromagnetic one.
2. Since the strong force is short range and attractive, the potential in which the nucleons exist is created by all the other nucleons in contrast to the force between the atomic electrons and the spatially separated positive charge of the nucleus.

Two fundamental models—the liquid-drop model and the shell model—represent key milestones in the development of understanding the nucleus. Their reconciliation explains many nuclear phenomena, particularly the emergence of magic numbers and the behavior of exotic nuclei.

1.1.1 The Liquid-drop Model

The liquid-drop model, first formulated comprehensively by Weizsäcker [2] and discussed in detail by Bethe and Bacher in 1936 [3], treats the nucleus analogously to a charged droplet of incompressible fluid. This model emphasizes collective properties of the nucleus, such as binding energy, surface tension, and Coulomb repulsion among protons.

The semi-empirical mass formula (also called the Bethe-Weizsäcker formula) captures essential trends:

$$B(A, Z) = a_V A - a_S A^{2/3} - a_C \frac{Z(Z-1)}{A^{1/3}} - a_A \frac{(N-Z)^2}{A} \pm \delta(N, Z)$$

where each term accounts for volume, surface, Coulomb, asymmetry, and pairing effects respectively.

While successful at explaining global nuclear properties—such as the approximate binding energy per nucleon—it could not account for observed anomalies in nuclear stability, such as nuclei at specific nucleon numbers (2, 8, 20, 28, 50, 82, 126) exhibiting enhanced stability: the magic numbers.

1.1.2 The Shell Model

The limitations of the liquid-drop model led to the proposal of the nuclear shell model, developed independently by Maria Goeppert Mayer [4] and by Haxel, Jensen, and Suess [5] in the late 1940s. Mayer and Jensen later collaborated on a comprehensive treatment of the model [6], and were jointly awarded the Nobel Prize in Physics in 1963 for their contributions. Their work, expanding on the early suggestions of Elsasser [7], showed that nucleons move in quantized energy levels within a mean potential well created by all other nucleons—analogueous to electrons in atomic orbitals.

Initially, it was thought that a simple three-dimensional harmonic oscillator potential could describe the structure. However, it was soon realized that including a strong spin-orbit coupling term, where the nucleon's spin couples to its orbital motion, was critical to reproduce the magic numbers observed experimentally [8].

In particular, spin-orbit splitting lifts the degeneracy of orbital states, energetically favoring high-angular-momentum states (e.g., $j = l + 1/2$), thus producing large energy gaps at specific nucleon numbers—those corresponding to the magic numbers. This effect is illustrated in Figure 1.1, which shows the rearrangement of single-particle levels and the resulting magic numbers emerging from spin-orbit coupling.

The modified energy level filling, based on this strong spin-orbit interaction, led to a successful explanation for the pronounced nuclear stability at nucleon numbers:

$$2, 8, 20, 28, 50, 82, 126$$

for both protons and neutrons separately [8].

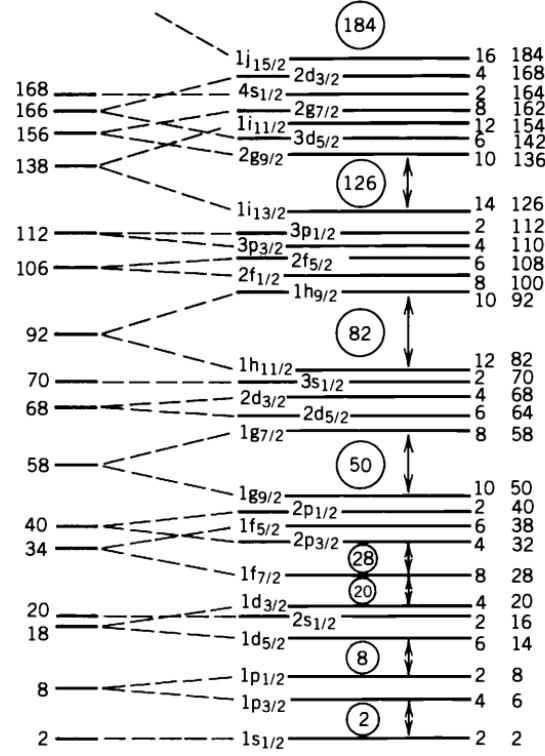


Figure 1.1: Single-particle shell model level scheme illustrating the origin of nuclear magic numbers after incorporating spin-orbit coupling. The diagram shows the energy splitting of nuclear orbitals due to spin-orbit interaction, leading to the observed magic numbers (circled) corresponding to closed shells at nucleon numbers 2, 8, 20, 28, 50, 82, 126, and 184. The levels are labeled with their orbital and total angular momentum quantum numbers nlj , and the associated degeneracy $(2j+1)$ is indicated on the right. Reprinted figure from Ref. [9]

1.1.2.1 Magic Numbers and Shell Closures

In the shell model:

- A closed shell means that all available states at a given energy are filled.
- Nuclei with both proton and neutron numbers equal to magic numbers (so-called doubly magic nuclei, e.g., ^{16}O , ^{208}Pb) exhibit especially high binding energies, spherical shapes, and relatively low excitation spectra.

Haxel, Jensen, and Suess [5] provided a succinct explanation showing how a strong spin-orbit coupling splits the energy levels such that filling up the states naturally reproduces the magic numbers.

1.1.2.2 Extension to Exotic Nuclei

The classic shell model was originally built based on stable and near- β -stable nuclei. However, advances in experimental techniques have allowed the study of exotic nuclei—nuclei far from stability, with unusual neutron-to-proton ratios.

In these systems [10]:

- Traditional magic numbers can weaken or even disappear .
- New magic numbers (e.g., $N = 16$, $N = 34$) can emerge.
- Nuclear deformations become more common, especially near the so-called "island of inversion" (around $N = 20$).
- Phenomena like neutron halos emerge.

This phenomena has led to the concept of shell evolution, where the shell structure depends on the balance between the nuclear force components (central, spin-orbit, and tensor interactions) and changes with proton-neutron ratios.

1.1.3 Conclusion

In summary, the liquid-drop model offered a macroscopic view of nuclear behavior, while the shell model introduced microscopic structure and quantization effects that explain nuclear stability at magic numbers. The discovery of exotic nuclei has highlighted that the shell structure itself is dynamic and evolves under extreme conditions, demonstrating the richness and complexity of nuclear structure beyond the stable valley.

The quest for obtaining a model that will adequately describe the nucleus in all areas of stability, as well as at the extremes of nuclear existence has been motivating the last 60 years of nuclear physics and has led to the designing of new laboratories, such as the the FAIR facility.

1.2 The FAIR Facility

The Facility for Antiproton and Ion Research (FAIR), currently under construction as an expansion to the existing GSI¹ in Darmstadt, Germany, represents one of the most ambitious research infrastructures worldwide for exploring the structure of matter and the evolution of the universe. FAIR will provide intense, high-quality beams of protons, antiprotons, and ions—ranging from hydrogen to uranium—enabling unique access to a wide range of unexplored regimes in hadronic, nuclear, atomic, and plasma physics, as well as interdisciplinary and applied sciences.

The FAIR accelerator complex, seen in Figure 1.2, is centered around the superconducting synchrotron SIS100 [11], which, with its 100 Tm magnetic rigidity and 1100 m circumference, will serve as the backbone for beam delivery. The accelerator system is complemented by specialized storage rings and the Super-FRS fragment separator [12], facilitating the production and manipulation of both stable and exotic radioactive beams

¹GSI Helmholtzzentrum für Schwerionenforschung

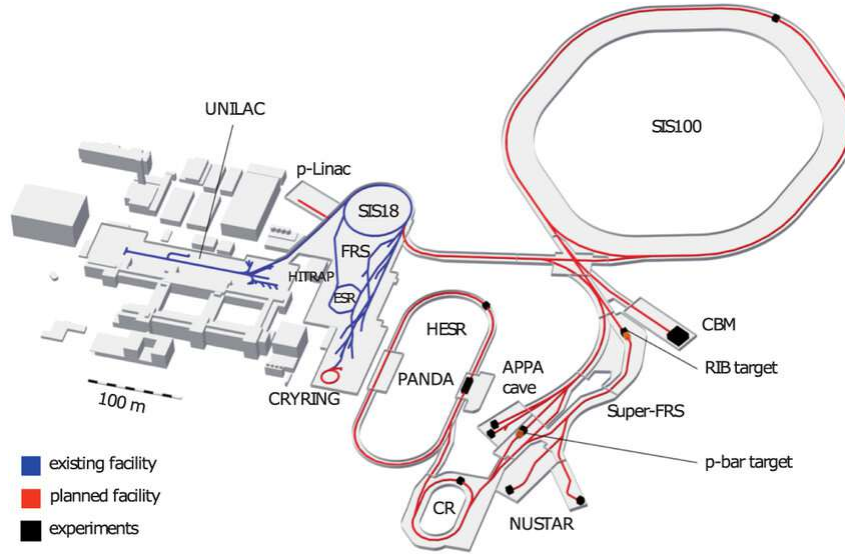


Figure 1.2: Layout of GSI-FAIR with the existing and planned beamlines shown in blue and red, respectively. The experimental sites are marked in black (figure: GSI Darmstadt). © Copyright: GSI/FAIR.

with intensities and purities that exceed those of existing facilities by several orders of magnitude.

FAIR's scientific program is structured around four foundational experimental pillars [13–15]:

- APPA – Atomic Physics, Plasma Physics, and Applications [16]

The APPA collaboration focuses on high-precision studies in atomic and plasma physics, particularly utilizing highly charged ions and high-intensity ion beams. This enables research into correlated electron dynamics under ultra-strong electromagnetic fields, tests of quantum electrodynamics (QED) in critical regimes, and the investigation of high energy density matter relevant to astrophysical phenomena and fusion technologies. APPA also addresses applied sciences such as materials modification and radiation biology under cosmic-ray-like ion bombardment.

- CBM – Compressed Baryonic Matter [17]

The CBM experiment aims to map the QCD phase diagram at high baryon densities and moderate temperatures, a region largely inaccessible to collider experiments like those at RHIC and LHC. Using high-intensity heavy-ion beams from SIS100, CBM will explore the properties of dense nuclear matter, the nuclear equation of state, and search for signals of deconfinement, chiral symmetry restoration, and the QCD critical point. It features the measurement of rare probes such as dileptons, open and hidden charm, and multi-strange hyperons with unprecedented statistics.

- PANDA – AntiProton ANnihilation at DArmstadt [18]

PANDA will utilize antiproton beams stored and cooled in the High Energy Storage Ring (HESR) to investigate the structure of hadrons and their interactions. Its focus includes charmonium spectroscopy, the identification of exotic states such as hybrids and glueballs, and studies of the hadron mass generation mechanism via gluonic dynamics. PANDA's precision measurements are expected to yield insights into the strong force at the confinement scale, extending beyond the capabilities of previous antiproton experiments.

- NuSTAR – Nuclear Structure, Astrophysics, and Reactions [19]

The NuSTAR collaboration (Nuclear Structure, Astrophysics and Reactions) lies at the heart of FAIR's mission to investigate nuclei far from stability and their relevance in cosmic nucleosynthesis. NuSTAR's scientific objectives include exploring the structure of nuclei near the drip lines, understanding the processes driving the astrophysical r-process, and studying fundamental interactions and symmetries through decay modes and reaction dynamics of exotic nuclei.

Central to NuSTAR is the Super-FRS, a high-resolution, multi-stage fragment separator designed to deliver intense, isotope-pure beams of radioactive ions. These beams will allow exploration of previously inaccessible regions of the nuclear chart. A vital component of NuSTAR is the Reactions with Relativistic Radioactive Beams (R³B) collaboration, which is dedicated to reaction studies in inverse kinematics using high-energy exotic nuclei. R³B will enable kinematically complete measurements of a wide variety of reaction channels (e.g., knockout, breakup, Coulomb excitation), providing deep insights into nuclear forces, shell evolution, and exotic decay modes. The R³B setup combines active and passive detectors in a versatile setup optimized for the coincident detection of charged particles, neutrons, and γ -rays.

1.3 Author's Contribution and Thesis Overview

Simulations for the experiment.

RPC preparation: Moved NeuLAND bar for calibration. Flashed RPC and inserted the gas mixture. Found working point.

Developed a script to monitor voltage and current in the RPC resistive plates.

Updated a script to power cycle RPC and reboot DAQ and Acquisition.

DIRECT REACTIONS AS SPECTROSCOPIC TOOLS

"The art of simplicity is a puzzle of complexity."

Douglas Horton

2.1 Introduction

The structure of atomic nuclei—how protons and neutrons arrange themselves in shells, how they correlate, and how these features evolve across the nuclear chart—has been at the heart of nuclear physics for decades. To unravel this structure, nuclear physicists have long relied on direct reaction mechanisms, in which a projectile interacts with a target nucleus in a controlled and selective way, producing clean signatures of specific internal configurations. Among these, transfer reactions and knockout reactions have historically provided the foundational experimental pathways for exploring the single-particle nature of the nucleus.

2.2 Transfer Reactions

Nucleon transfer reactions, such as (d,p) , (p,d) , or (t,α) , involve the exchange of one or more nucleons between the projectile and the target. In the classic (d,p) reaction, for instance, a neutron is transferred from a deuteron to the target nucleus, leaving the residual system in a state that reveals the properties of the added neutron orbital.

These reactions have played a central role in defining the shell model: by measuring angular distributions and comparing them to reaction theory (e.g., using the distorted wave Born approximation, DWBA), one can extract:

- The orbital angular momentum l of the transferred nucleon (via angular distribution patterns).
- The spectroscopic factor, quantifying the overlap between the initial and final nuclear states.

Transfer reactions are best suited for stable or long-lived nuclei at relatively low energies (5–50 MeV/u), where they benefit from high cross-sections and well-developed theoretical frameworks [20]. However, they become experimentally challenging for short-lived isotopes and high- Z systems, especially where targets cannot be fabricated.

2.3 Knockout Reactions

With the advent of radioactive beam facilities, transfer methods began to be complemented—and in some cases replaced—by nucleon knockout reactions, particularly in inverse kinematics. In a knockout reaction, such as $(A, A-1)$, a high-energy projectile nucleus collides with a light target (e.g., ${}^2\text{Be}$, C, or H), and a single nucleon is suddenly removed from the projectile.

Knockout reactions operate in the sudden approximation: the interaction is fast enough that the removed nucleon doesn't reconfigure its wavefunction during the process. The resulting residual nucleus and its kinematics encode the structural information of the pre-existing configuration.

By measuring the momentum distribution of the residual fragment and comparing it with theoretical predictions (e.g., via the eikonal reaction model or Glauber theory), one obtains:

- The l -value of the knocked-out nucleon (from the width and shape of the distribution).
- The spectroscopic strength, linked to orbital occupancy.

Knockout reactions revolutionized structure studies of exotic nuclei, especially those near the drip lines, by enabling measurements of systems that could only be formed in-flight.

2.4 From Knockout to Quasi-Free Scattering

While both transfer and knockout reactions have yielded profound insights, their selectivity and interpretability face limitations. Transfer reactions are constrained by target availability and are often restricted to stable systems. Knockout reactions, although experimentally versatile, involve complex reaction dynamics with model dependencies that grow in neutron-rich environments and at higher energies.

To transcend these limitations, quasi-free scattering has re-emerged as a uniquely powerful probe. Conceptually close to knockout, but kinematically richer and theoretically cleaner in many regimes, quasi-free scattering reactions like $(e,e'p)$ and $(p,2p)$ offer direct access to the momentum and separation energy of individual nucleons in their initial nuclear orbitals. In high-energy kinematics, and under the impulse approximation, the

scattering process isolates the interaction between the probe and a single nucleon, while the remaining nucleus acts as a spectator.

This progression—from transfer, to knockout, to quasi-free scattering—represents not just an evolution of experimental technique, but a deepening of our ability to map the quantum landscape inside the nucleus, from its shell structure to the underlying many-body correlations.

2.5 Quasi-free Scattering Reactions

2.5.1 Introduction to Quasi-Free Scattering

Quasi-free Scattering (QFS) has emerged as one of the most powerful tools in nuclear physics to probe the single-particle structure and correlations within atomic nuclei. It encompasses a class of reactions in which an incident probe (either an electron or a proton) interacts predominantly with a single nucleon in the nucleus, while the remaining nucleons act as passive spectators. Under kinematic conditions favoring large momentum and energy transfer, and small final-state interactions (FSI), the process can be approximated by the impulse approximation (IA)—a simplification in which the nuclear many-body system is treated as a collection of quasi-free, independent nucleons.

2.5.2 Historical Context and the Electron-Induced Paradigm

The conceptual and experimental foundations of QFS were established in the 1960s, particularly with the pioneering review by Jacob and Maris (1966) [21], which systematized the theoretical framework for electron-induced QFS reactions of the type $(e,e'p)$. In these reactions, a high-energy electron transfers a well-defined amount of momentum and energy to a proton within the target nucleus, which is then ejected and detected in coincidence with the scattered electron. The kinematic constraints of such experiments enable the reconstruction of the missing energy and momentum of the ejected nucleon, which provides a direct spectroscopic window into the bound-state wavefunction.

This formalism was further refined in the 1973 follow-up by the same authors [22], which accounted for distortions in both the incoming and outgoing waves due to the nuclear potential—introducing the Distorted Wave Impulse Approximation (DWIA). These early $(e,e'p)$ experiments, primarily conducted at SLAC and Saclay, provided critical benchmarks for understanding shell structure, spectroscopic factors, and occupancy probabilities, particularly in medium-mass nuclei like ^{16}O and ^{40}Ca . However, the method remained largely confined to stable nuclei due to the limitations in electron beam-target combinations.

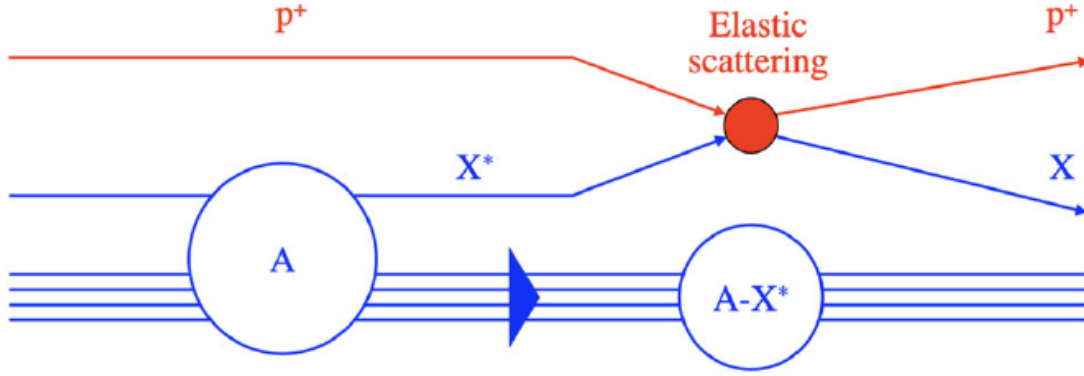


Figure 2.1: Schematic diagram of a QFS reaction induced by a proton p^+ on a nucleus A via elastic scattering off the virtual constituent particle X^* . Three real particles are generated in the final state: the scattered proton p^+ , the knock-out cluster X and the spectator nuclear fragment ($A-X^*$). Reprinted figure from Ref. [24]

2.5.3 Proton-Induced QFS and DWIA Evolution

In parallel, the use of proton-induced QFS—such as $(p,2p)$ or (p,pn) reactions—gained traction as an alternative means to probe the same physics with hadronic probes [23]. While the complexity of the nucleon-nucleon (NN) interaction and stronger final-state interactions initially complicated the analysis, the development of DWIA for hadronic probes enabled the extraction of momentum distributions and spectroscopic observables with comparable reliability. These reactions offered higher cross-sections and better experimental accessibility, though at the cost of increased theoretical uncertainty due to ambiguities in the NN scattering amplitude and optical potentials.

2.5.4 The Modern Era: Inverse Kinematics and Exotic Nuclei

A transformative leap occurred in the 21st century with the advent of inverse kinematics QFS using radioactive ion beams (RIBs) and hydrogen targets. As comprehensively reviewed by Panin et al. (2021) [24], modern QFS experiments at facilities such as RIKEN, GSI/FAIR, and FRIB utilize high-energy beams of neutron- or proton-rich nuclei impinging on proton-rich targets. The resulting reactions—such as $(p,2p)$, (p,pn) , or $(p,p\alpha)$ —enable the study of short-lived and exotic systems far from stability, including halo nuclei, nuclei near the neutron drip line, and those within the so-called "island of inversion."

These experiments exploit complete kinematic reconstruction techniques, coincident γ -ray detection, and high-resolution tracking of all final-state particles. This allows the identification of orbital angular momentum (l) of removed nucleons via momentum distributions, providing a model-independent probe of nuclear shell structure. Moreover, inverse kinematics QFS has facilitated the spectroscopy of unbound states, the quantification of short-range correlations (SRCs) [25–27], and insights into clustering phenomena in

light and medium-mass nuclei [28–30].

2.5.5 Benchmark and Current Frontiers

QFS today occupies a unique position among reaction mechanisms, bridging single-particle and correlated many-body dynamics. Benchmarked by decades of electron-induced QFS data, modern $(p, 2p)/(p, pn)$ measurements are now used to:

- Test shell evolution in neutron-rich isotopes.
- Quantify spectroscopic factors and their reduction (quenching).
- Investigate SRCs in asymmetric nuclear matter.
- Map the extent of the island of inversion.
- Explore the nature of unbound and resonant nuclear states.

Theoretical advancements, notably the eikonal DWIA and relativistic frameworks, allow consistent comparisons between experiment and shell-model or *ab initio* structure predictions. Future developments—such as the integration of machine learning in reaction theory, or the use of polarized beams and targets—promise even finer resolution of nuclear substructure.

EXPERIMENT

"Somewhere, something
incredible is waiting to be
known."

Carl Sagan

3.1 Context and Goal of the Experiment

The proposed experiment, detailed in research proposal G-24-00249 [31], aims to investigate the structure of the neutron-rich fluorine isotope, ^{25}F , through one-proton knockout reactions. This study is motivated by the "drastic extension of the neutron drip line for $Z=9$ compared to $Z=8$ isotopes," a phenomenon that remains poorly understood [32]. The experiment seeks to elucidate how the ^{24}O core is polarized by the presence of an additional proton in ^{25}F , thereby shedding light on the mechanisms responsible for the observed drip line extension.

The experiment will employ the quasi-free scattering (QFS) reaction $^{25}\text{F}(p,2p)^{24}\text{O}$ in inverse kinematics, effectively knocking out a deeply bound valence proton from the ^{25}F nucleus [33]. This approach will utilize the R³B experimental setup, including the high-efficiency neutron detector NeuLAND [34], to achieve complete kinematic measurements and obtain accurate spectroscopic information on the populated final states of ^{24}O . By analyzing the experimental data, researchers aim to determine the extent to which the single $d_{5/2}$ proton in ^{25}F modifies the structure of the core nucleons, potentially indicating deformation or polarization of the ^{24}O core [35].

Ultimately, the goal of this experiment is to provide a more detailed understanding of the nuclear structure of neutron-rich fluorine isotopes and the underlying reasons for the extended neutron drip line at $Z=9$. The results will contribute to a more comprehensive picture of nuclear forces and structure in exotic nuclei, addressing a fundamental question in nuclear physics.

ADD IMAGE OF ISOTOPE CHART SHOWCASING THE DIFFERENCE IN THE NEUTRON DRIP LINE

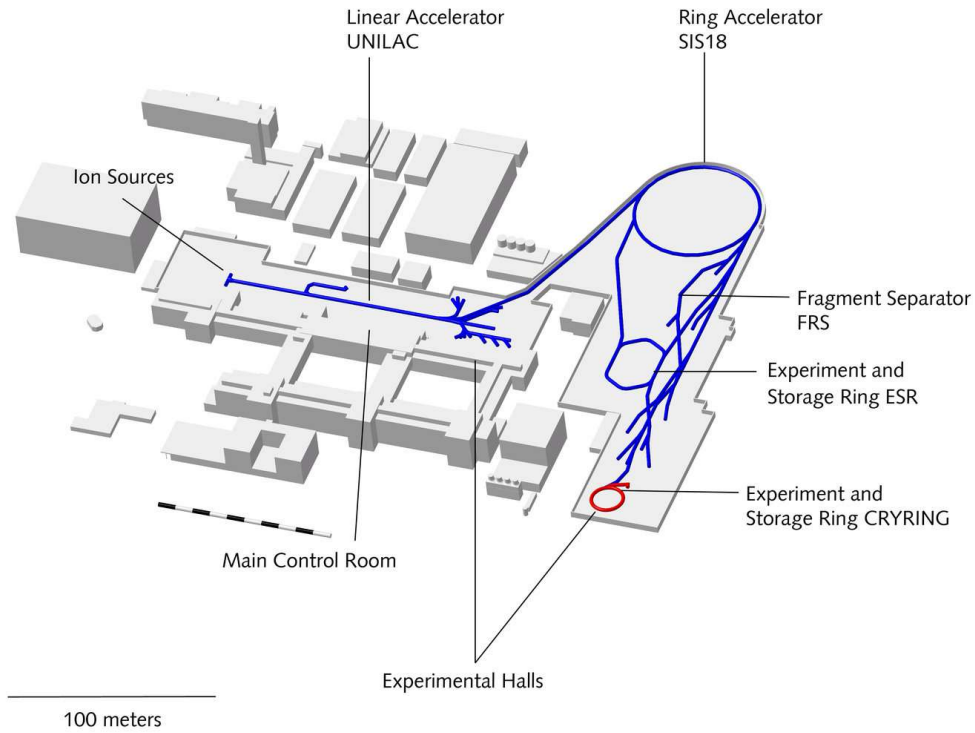


Figure 3.1: Schematic layout of the GSI Helmholtzzentrum accelerator facility. The diagram shows the major components including the ion sources, the UNILAC linear accelerator, the SIS18 synchrotron, the Fragment Separator (FRS), and the associated experimental halls [36].

3.2 The GSI Accelerator System

Annex I

The previously described experiment will take place at the GSI Helmholtzzentrum für Schwerionenforschung in Darmstadt, Germany. GSI's accelerator complex, seen in Figure 3.1, provides the infrastructure required to produce and deliver rare isotope beams, such as ^{25}F , for inverse kinematics reactions. The R³B setup, located in Cave C downstream of the FRS, enables complete kinematic reconstruction, making it well-suited for the spectroscopic investigation of exotic nuclei. The following sections outline the accelerator chain that delivers these beams—from ion production through the UNILAC and SIS18 to the FRS and the experimental area.

3.2.1 From Source to Experimental Cave

3.2.1.1 Ion Production

The accelerator cycle begins with the production of ions in specialized ion sources. Depending on the experimental requirements, different types of sources are used, including

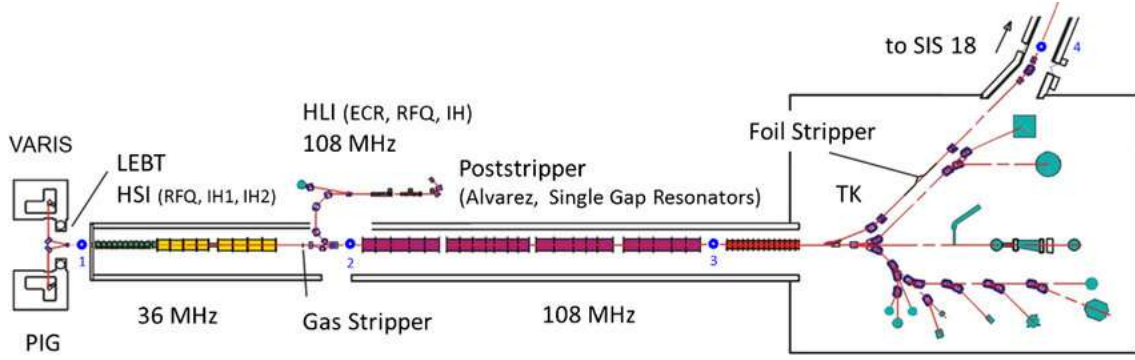


Figure 3.2: Detailed schematic of the UNILAC accelerator. The figure highlights the beamline structure from ion sources through the High Current Injector (HSI), Radio-Frequency Quadrupole (RFQ), Interdigital H-mode Drift Tube Linacs (IH-DTL), gas stripper section, Alvarez Drift Tube Linac (DTL), and the transfer line to SIS18. Beam diagnostic and stripping sections are also labeled [39].

electron cyclotron resonance (ECR) sources and Penning ion sources [37]. These generate high charge state ions by stripping electrons from atoms in a plasma environment. The produced ions are pre-accelerated and then injected into the linear accelerator for further acceleration.

3.2.1.2 The UNILAC

The Universal Linear Accelerator (UNILAC) [38] serves as the primary injector for the GSI accelerator chain. It accelerates ions to energies of several MeV/u before their injection into the synchrotron. Structurally, the UNILAC consists of several stages: a radio-frequency quadrupole (RFQ), an interdigital H-mode drift tube linac (IH-DTL), and a transfer line to the synchrotron SIS18 [39]. Over the years, substantial upgrades have been implemented to accommodate high-intensity beams and improve the beam quality for heavy ion acceleration. The layout of the UNILAC and its role as the front-end of the accelerator chain is depicted in Figure 3.2.

3.2.1.3 The SIS18

Following pre-acceleration by the UNILAC, ion beams are injected into the SIS18 synchrotron [40], where they are further accelerated to relativistic energies. The SIS18 is a fast-cycling synchrotron with a magnetic rigidity of up to 18 Tm, capable of accelerating ions to several hundred MeV/u. It incorporates sophisticated beam manipulation techniques including bunch compression and multiturn injection to optimize performance and beam delivery. Figure 3.3 illustrates the SIS18 layout and its specifications. The synchrotron serves both as a terminal accelerator for in-house experiments and as an injector for future FAIR components.

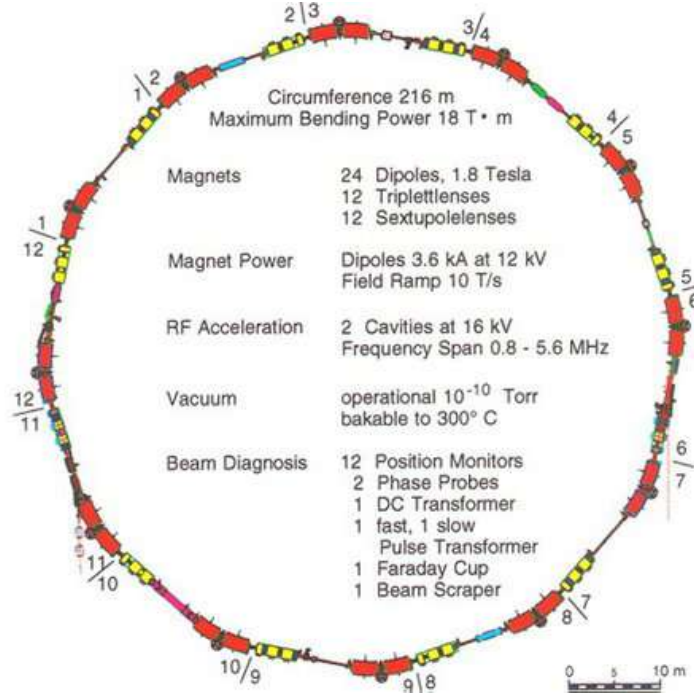


Figure 3.3: Plan view of the SIS18 heavy-ion synchrotron, illustrating its 12 identical lattice sections, dipole and quadrupole magnet configurations, RF acceleration cavities, and positions of beam diagnostic systems [41].

3.2.1.4 The Fragment Separator (FRS)

High-energy ions exiting the SIS18 are directed to the FRagment Separator (FRS) [42], a magnetic spectrometer designed for in-flight separation of rare isotopes. The FRS exploits differences in magnetic rigidity and energy loss to isolate specific nuclear species from a cocktail beam. It comprises four dipole magnets forming a two-stage separation system and includes focal planes for tracking, time-of-flight, and energy-loss measurements. As shown in Figure 3.4, the FRS facilitates beam transport from SIS18 to various experimental areas, enabling studies of exotic nuclei and reaction mechanisms.

3.2.1.5 Experimental Caves

Following separation in the FRS, ion beams are directed toward a suite of experimental stations, commonly referred to as experimental caves. These caves are equipped for diverse research programs ranging from nuclear structure and astrophysics to plasma physics and medical applications. One of the principal experimental areas is Cave C, located directly downstream of the FRS. This cave is the one that hosts the R³B setup.

Cave C serves as a prototype environment for the future NUSTAR experiments at FAIR. Specifically, the R³B instrumentation and experimental approach implemented at GSI are being used to develop and validate detector technologies and methodologies for the NUSTAR Cave under construction at FAIR. This strategic continuity ensures a seamless transition of experimental capabilities and scientific objectives from the current

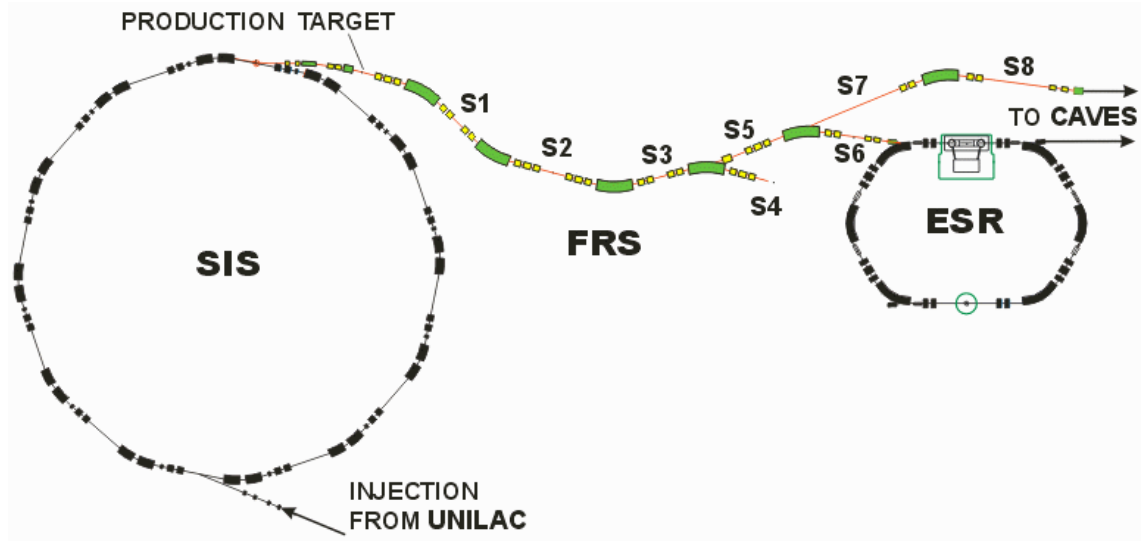


Figure 3.4: Schematic of the FRS system showing its dipole magnet sections, dispersive and achromatic focal planes (F1–F8), and the separation of rare isotope beams. The figure also shows the branching to dedicated experimental areas, including the Direct Branch, Ring Branch (ESR), and the experimental caves [43].

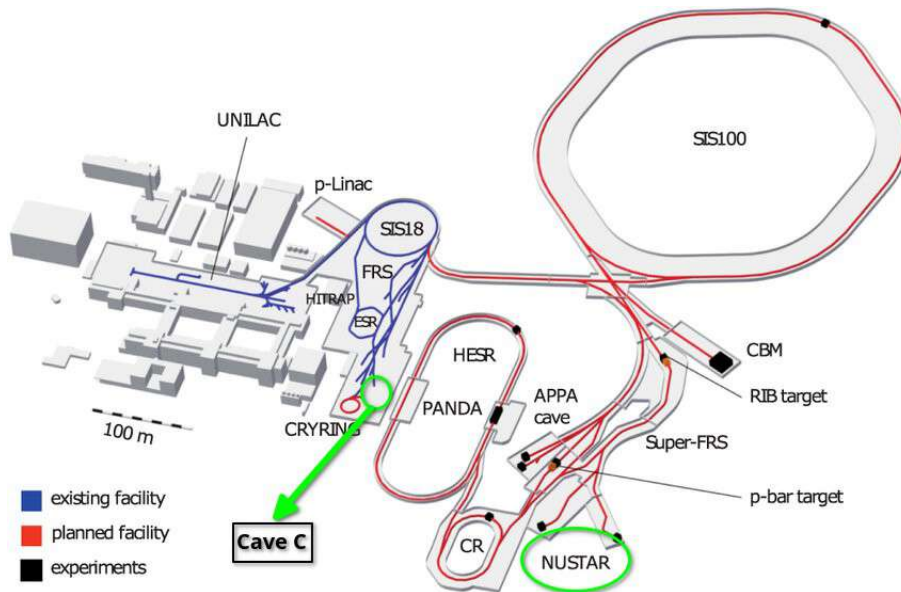


Figure 3.5: Layout of GSI-FAIR with Cave C highlighted, where the prototype of the future NUSTAR R³B setup stands and where the present experiment took place.

GSI facility to the FAIR complex.

The overall layout of the GSI accelerator chain and its future integration with FAIR, including the locations of Cave C and the planned NUSTAR cave, is illustrated in Figure 3.5.

²⁴ Ne	²⁵ Ne	²⁶ Ne	²⁷ Ne	²⁸ Ne	²⁹ Ne
		4.47e-1 0.003%	3.19e+1 2.364%	7.94e+0 8.192%	2.57e-2 0.446%
²³ F	²⁴ F	²⁵ F	²⁶ F	²⁷ F	
1.19e-1 2e-4%	4.12e+1 0.7%	3.1e+1 6.879%	2.86e-1 1.028%	7.93e-6 5.6e-4%	
²² O	²³ O	²⁴ O			
1.04e+2 4.561%	2.21e+0 1.471%	5.14e-4 0.006%			

Figure 3.6: Expected secondary cocktail beam of ^{25}F in Cave C as obtained by LISE++ calculations. The numbers under the names of isotopes indicate calculated rates per second. Reprinted figure from Ref. [31].

3.2.1.6 Summary

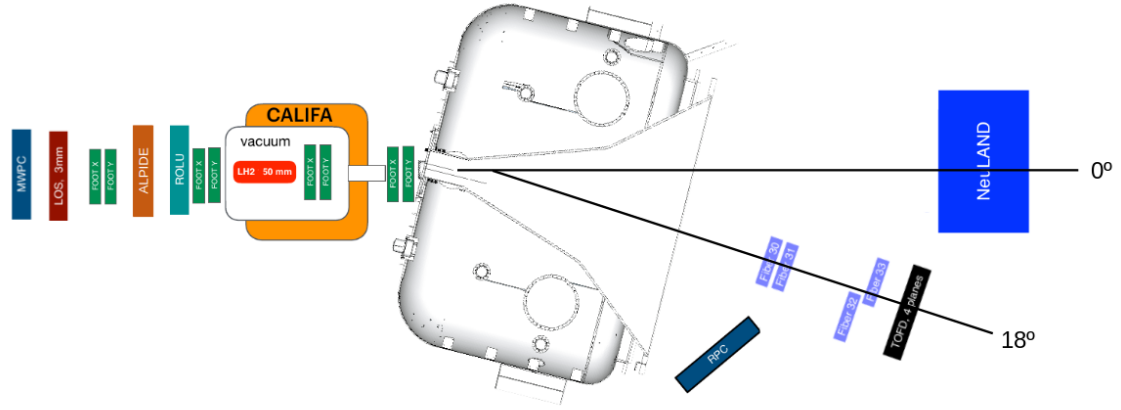
The GSI accelerator system exemplifies a complex yet highly coordinated infrastructure, progressing from ion production through successive acceleration stages and culminating in precision experiments. The integration of the UNILAC, SIS18, and FRS ensures the delivery of high-intensity, high-quality ion beams, establishing GSI as a cornerstone of heavy ion research.

3.2.2 Beam used in Experiment

In the proposed experiment [31], a ^{40}Ar primary beam with an energy of 700 MeV/u is employed to produce a secondary beam containing the ^{25}F isotope of interest. The primary beam impinges on a beryllium target located at the FRS, inducing nuclear fragmentation reactions. This process generates a cocktail beam consisting of various isotopes, including ^{25}F , which is then selected and guided towards the experimental setup in Cave C.

The FRS is used to separate and purify the secondary beam, ensuring a sufficient intensity of ^{25}F for the subsequent experiment. As seen in Figure 3.6, LISE++ simulations, using the EPAX3.1a production model, predict an intensity of approximately 30 ions per second (pps) of ^{25}F on the secondary target [31]. The total intensity of the secondary cocktail beam in Cave C is expected to be below 700 pps, with a purity of around 5% for ^{25}F [31]. The relatively low total intensity allows for data acquisition without significant downscaling of triggers and minimizes dead time.

In Cave C, the ^{25}F secondary beam interacts with a liquid hydrogen (LH2) target, which serves as the reaction target for the one-proton knockout reaction $^{25}\text{F}(p,2p)^{24}\text{O}$. The LH2 target is positioned in the center of the CALIFA calorimeter, enabling the detection of outgoing protons from the reaction. The use of a 150 mm thick LH2 cell was initially planned but, due to problems in the liquefaction phase, the cell was replaced for a 50 mm one, reducing the reaction yield.

Figure 3.7: Sketch of the experimental setup at R³B.

3.3 R³B Setup

The R³B (Reactions with Relativistic Radioactive Beams) setup at GSI is designed for high-precision, kinematically complete measurements of nuclear reactions involving rare isotope beams at relativistic energies. For the investigation of the $^{25}\text{F}(p,2p)^{24}\text{O}$ reaction, the configuration is optimized to detect all relevant particles emerging from the target—charged fragments, recoil protons, and neutrons—with high resolution and full angular coverage. The following description reflects the actual experimental layout, based on the schematic shown in Figure 3.7, and supported by the experimental proposal and detector-specific references.

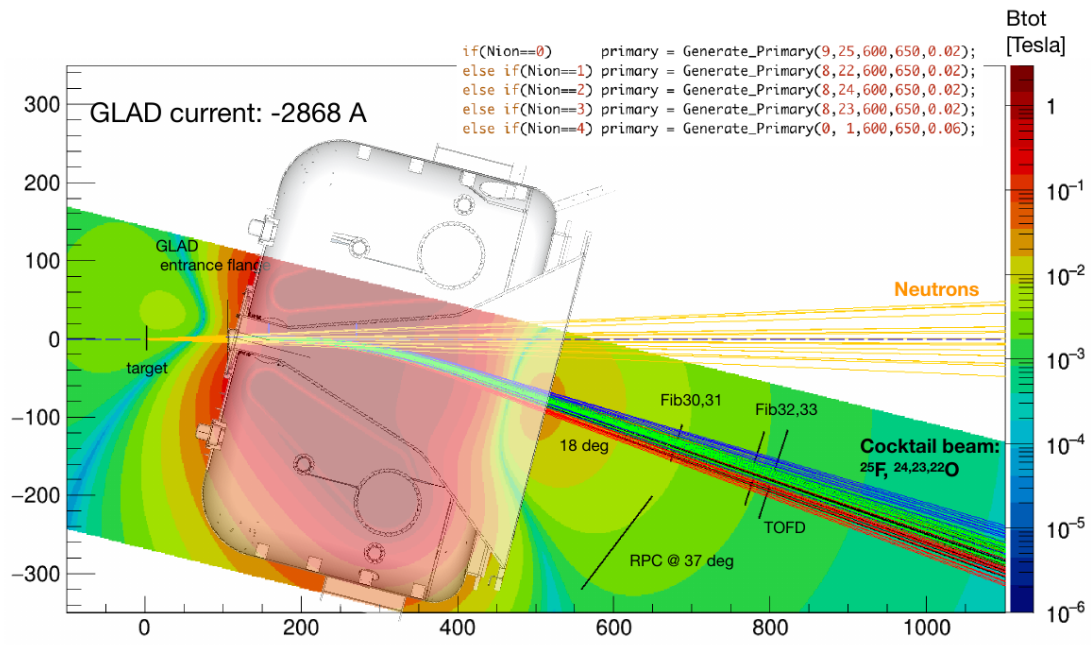
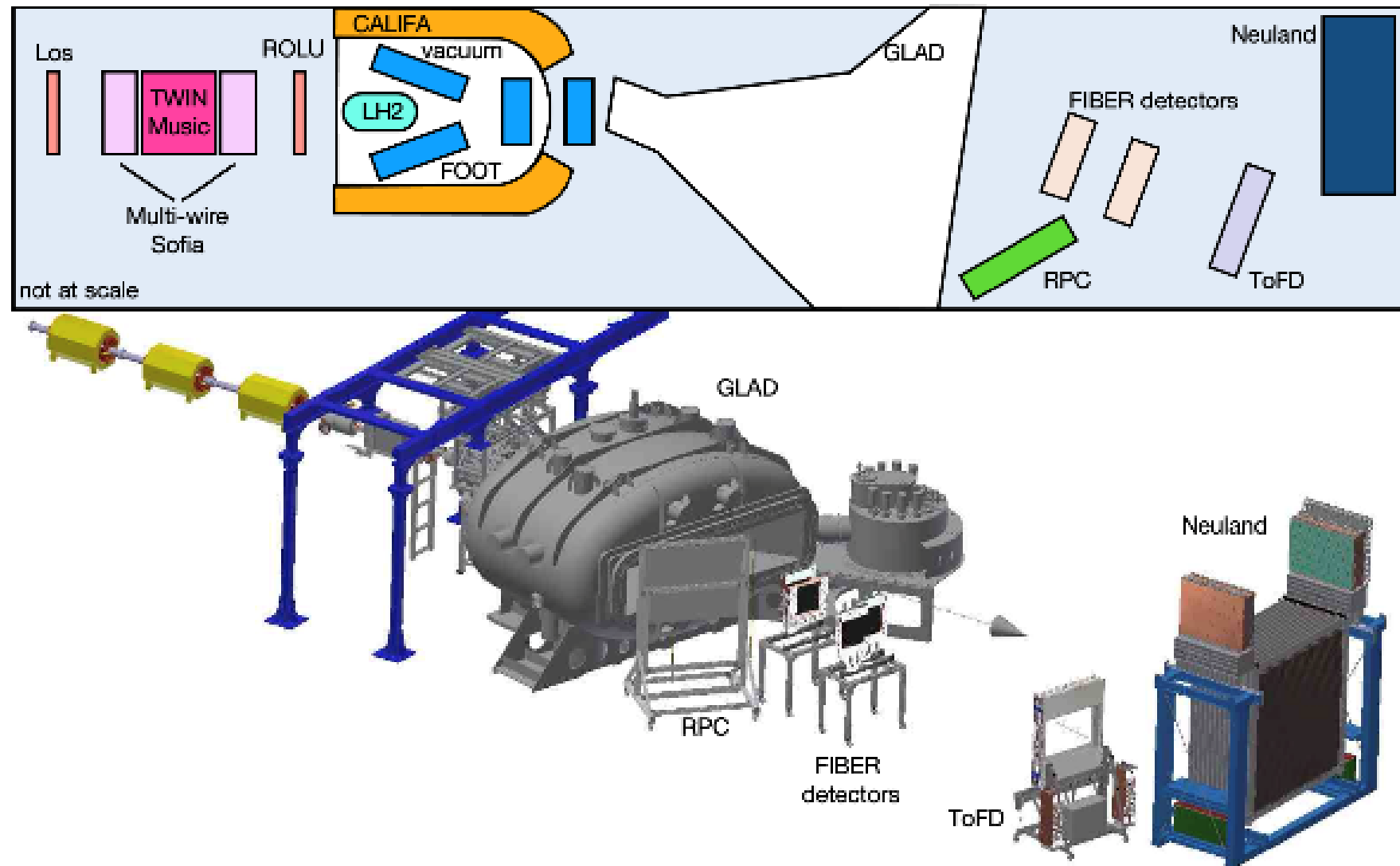


Figure 3.8: Simulated trajectories through the GLAD magnet. The color map indicates the magnetic field of the magnet. The LH2 target is located at the (0,0,0) point in front of GLAD. Reprinted figure from Ref. [31].



20
Figure 3.9:

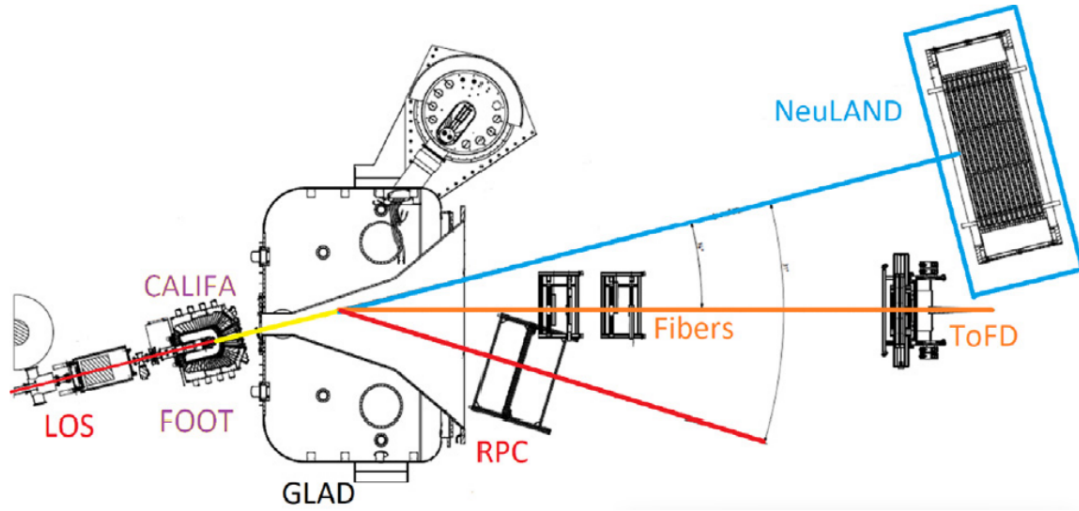


Figure 3.10: Schematic representation of the R³B setup with beam lines.

R³B

R³B

Time-of-Flight Detector (ToFD)

ToFD

New Large-Area Neutron Detector (NeuLAND)

NeuLAND

GSI Large Acceptance Dipole (GLAD)

GLAD

CALorimeter for In-Flight detection of gamma-rays and charged pArticles (CALIFA)

CALIFA

Resistive Plate Chamber (RPC)

RPC

3.3.1 Role of each detector

ALPIDE [44].

3.3.1.1 Incoming Beam Tracking and Identification

The secondary beam of ²⁵F enters the experimental area and is tracked and identified using a series of detectors placed along the beamline. The first two components, **MWPC0** and **MWPC1**, are multi-wire proportional chambers that provide precise position and angular information of the incoming ions with minimal material budget. This tracking is essential for reconstructing the reaction vertex within the extended target and for correlating the incoming ion with its downstream reaction products [45].

Following these are the **TwinMUSIC** chambers, a dual-section ionization detector that measures the energy loss (ΔE) of incoming particles to determine their nuclear charge (Z). This is especially important in purifying the cocktail beam and identifying the rare ^{25}F ions on an event-by-event basis.

Immediately downstream of TwinMUSIC is the **LOS** (Large-area Organic Scintillator), which functions as the start detector for time-of-flight (ToF) measurements and provides an additional layer of Z identification via fast plastic scintillation. It also contributes to triggering logic for reaction events [31].

The final upstream detector before the target is **ROLU**, a collimating slit used to define the spatial beam profile and eliminate halo components. While not used for measurement directly, it is essential for ensuring clean beam passage into the reaction chamber.

3.3.1.2 Target Region

The nuclear reaction takes place inside a 50 mm liquid hydrogen (LH_2) target, located at the center of the setup. This thick cryogenic target is ideal for maximizing reaction yields in low-intensity beams, especially for quasi-free scattering processes like $(p,2p)$ in inverse kinematics. The outgoing protons and reaction residues emerge from the target into a nearly 4π detection environment.

Surrounding the target is **CALIFA** (CALorimeter for In-Flight particles and γ -rays), a highly segmented electromagnetic calorimeter composed of CsI(Tl) crystals. CALIFA plays a dual role: it detects prompt γ -rays from de-exciting nuclei and captures recoil protons from the $(p,2p)$ process. Its barrel geometry provides angular resolution suitable for identifying proton pairs and determining their opening angles, which are key to selecting quasi-free events. The energy resolution is approximately 5–6% at 1 MeV, and the time resolution is sub-nanosecond, enabling precise event reconstruction [46].

3.3.1.3 Fragment Tracking Before and After the Magnet

Charged reaction fragments are tracked using **FOOTs** (Fast Outgoing Object Trackers), which are double-sided silicon-strip detectors. The first pair of FOOTs (X and Y planes) is positioned directly downstream of the target, inside the CALIFA chamber, while the second pair is located just after CALIFA. These detectors provide position, angle, and energy-loss measurements, facilitating both trajectory reconstruction and Z identification of heavy residues such as ^{24}O , ^{23}O , and ^{22}O [31].

3.3.1.4 Magnetic Analysis with GLAD

After exiting CALIFA and the second FOOT pair, the charged fragments enter the field of **GLAD** (GSI Large Acceptance Dipole), a superconducting dipole magnet with a large aperture and strong bending power (up to 1.6 T·m). In this experiment, GLAD is operated at approximately 58% of its maximum field, providing sufficient magnetic rigidity to

separate fragments by momentum and charge state. This is critical for enabling invariant-mass spectroscopy when combined with tracking and time-of-flight measurements.

3.3.1.5 Downstream Fragment Tracking and Identification

Charged fragments deflected by GLAD are further tracked by **MWPC3**, a large-area proportional chamber providing coarse but wide-angle position measurements. This is followed by two layers of scintillating fiber detectors, which deliver fine spatial resolution (100 μm) for trajectory reconstruction and angular correlation. These tracking elements allow for precise determination of deflection angles, and thus of the total momentum vectors of the reaction products.

At the far end of the fragment line is the **ToFD** (Time-of-Flight Detector), a large-area plastic scintillator wall composed of four vertical planes. ToFD measures both ToF and energy loss with high precision, achieving timing resolutions of approximately 14 ps per plane and ΔE resolution better than 1% for Z determination. This data, combined with magnetic rigidity and tracking information, enables full fragment identification in both charge and mass number [47].

3.3.1.6 Neutron Detection with NeuLAND

Neutral particles emitted in the reaction, primarily neutrons from unbound states of ^{24}O and lighter oxygen isotopes, travel unaffected by GLAD's magnetic field and continue on a straight path to the **NeuLAND** (New Large-Area Neutron Detector). NeuLAND is composed of 3000 plastic scintillator bars arranged in 30 double planes, positioned approximately 15–35 meters downstream of the target at zero degrees. It is optimized for detecting fast neutrons (100–1000 MeV) with high efficiency (93–95% for single neutrons) and excellent spatial (1.5 cm) and timing (<150 ps) resolution [34].

NeuLAND enables measurement of multi-neutron events (e.g., $^{23}\text{O} + \text{n}$, $^{22}\text{O} + 2\text{n}$) via time-of-flight and interaction point reconstruction, and is critical for the invariant-mass reconstruction of the unbound final states populated in the (p,2p) reaction. This functionality allows the extraction of excitation energies and decay modes of exotic oxygen isotopes with unprecedented precision.

3.3.2 Particular Role of RPC

[48]

3.3.3 Main DAQ

Each detector is connected to the main Data Acquisition (DAQ), everytime they have a trigger, they send a trigger request to the main DAQ. If multiple detectors send a trigger request, it is considered an event to register and the main DAQ sends an accept signal, allowing every detector to save that signal.

All of these saved signals of each detector are then saved in a common *lmd* file containing every detectors data separated by event.

There's a synchronization signal with around 10 Hz to make sure every detector is synchronized.

3.4 Personal Contribution to the Experiment

"What we observe is not nature itself, but nature exposed to our method of questioning."

Werner Heisenberg

"The scientist is not a person who gives the right answers, but one who asks the right questions — and builds the tools to answer them."

Claude Lévi-Strauss
(paraphrased)

"Precision is not just about measurement — it is about insight."

4.1 History of RPCs/ Introduction

4.2 Properties

4.3 Build (components, electronics, gas mixture, DAQ, etc.)

DAQ

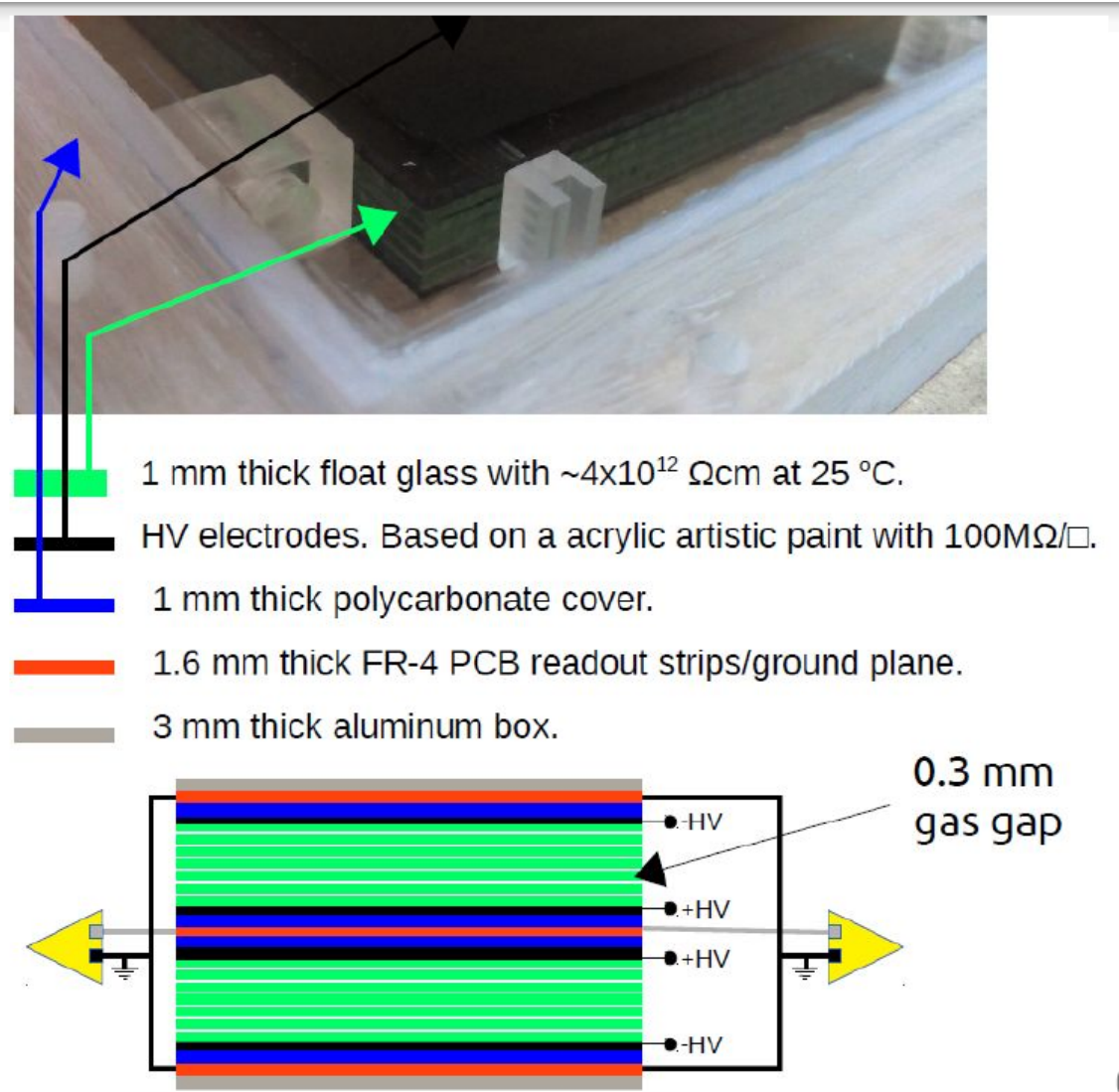


Figure 4.1: Schematic representation of the top view of the RPC.

4.3.1 RPC Build

- Active area of $1550 \times 1250 \text{ mm}^2 = 1.9 \text{ m}^2$.
- Two modules composed 6 gap RPC glass stacks.
- Gas mixture of $\text{C}_2\text{H}_2\text{F}_4$ (98%) and SF_6 (2%).
- Readout strips 3 cm width (placed in the middle of the two modules).
- Readout in both sides of the strips

4.3.2 RPC Electronics

4.3.3 RPC Gas Mixture

4.3.3.1 Pressure

The working pressure inside the chamber is lower than atmospheric pressure. This ends up being helpful because the atmospheric pressure itself compresses the RPC and makes everything tidy, aligned and without gaps.

4.3.3.2 Understanding the Role of the Gas Mixture in Resistive Plate Chambers (RPCs)

The gas mixture used in the Resistive Plate Chamber (RPC) at R³B consists of:

- 98% C₂H₂F₄ (Tetrafluoroethane, also known as R-134a, or Freon).
- 2% SF₆ (Sulfur Hexafluoride).

This specific gas combination plays a critical role in ionization, charge transport, avalanche formation, and quenching mechanisms inside the RPC. Below, the physics behind each component and their contributions to RPC performance are presented.

4.3.3.3 Role of C₂H₂F₄ (Tetrafluoroethane - Freon)

Primary Function: Ionization Medium and Avalanche Formation

C₂H₂F₄ is the main working gas, meaning that it provides the environment in which the ionization and charge multiplication take place.

Key Physics:

1. Ionization by Charged Particles

- When a charged particle (e.g., a proton, electron, or ion) passes through the RPC, it ionizes the gas molecules, creating free electrons and positive ions.
- The number of ionization events depends on the stopping power (dE/dx) of the particle.

2. Electron Acceleration and Avalanche Formation

- The electric field inside the RPC accelerates the free electrons, leading to electron impact ionization.
- This results in an avalanche process, where an initial electron triggers a chain reaction of ionization events.
- C₂H₂F₄ has a moderate first ionization energy (11.7 eV), making it an efficient medium for this multiplication process.

3. High Electron Attachment and Low Diffusivity

- Unlike noble gases (which have high electron mobility), $C_2H_2F_4$ has moderate electron attachment properties.
- This prevents excessive diffusion of electrons, leading to more localized avalanches.
- The electron mean free path is controlled to ensure controlled charge multiplication.

Why $C_2H_2F_4$ is Used Instead of Noble Gases?

- Noble gases like argon have too high a mobility, leading to excessive charge spread and loss of spatial resolution.
- $C_2H_2F_4$ is a polyatomic gas, meaning that it has multiple molecular vibrational modes, which help in absorbing excess energy and controlling the growth of the avalanche.

4.3.3.4 Role of SF_6 (Sulfur Hexafluoride)

Primary Function: Quenching Agent and Sparking Suppression

Although only 2% of the mixture, SF_6 is crucial for ensuring that the detector operates in a controlled avalanche mode rather than a full electrical breakdown (streamer mode).

Key Physics:

1. Electron Capture and Avalanche Control

- SF_6 is a strong electronegative gas, meaning it has a very high affinity for capturing free electrons.
- This limits the size of the avalanche, preventing uncontrolled charge growth.
- By capturing electrons, SF_6 reduces the risk of streamer formation, which would cause sparking and damage the RPC.

2. Suppression of Discharges

- SF_6 raises the dielectric strength of the gas mixture.
- This prevents full electrical breakdown, where a single avalanche could trigger an arc discharge across the plates.

3. Quenching of Excited Molecules

- SF_6 also helps in the de-excitation process by absorbing excess energy from excited $C_2H_2F_4$ molecules.
- This prevents UV photon emission, which could trigger secondary avalanches and reduce timing resolution.

4.3.3.5 RPC Operating Regimes and How the Gas Mixture Affects Them

Three Operating Modes of an RPC:

1. Avalanche Mode (Preferred Mode)

- The gas mixture ensures that charge multiplication occurs in a localized and controlled way.
- SF_6 limits the avalanche size, allowing the detector to operate in a stable mode with high timing precision.

2. Streamer Mode (Unwanted)

- If SF_6 were absent or insufficient, excessive charge buildup could lead to a transition from an avalanche to a streamer discharge.
- This would reduce spatial resolution and could permanently damage the RPC electrodes.

3. Breakdown Mode (Detector Failure)

- If the gas mixture fails to prevent excessive charge growth, the detector enters a self-sustaining discharge, which can permanently damage the plates.

4.3.3.6 Final Thoughts

This 98% $\text{C}_2\text{H}_2\text{F}_4$ + 2% SF_6 mixture is carefully chosen to:

- Optimize avalanche growth for fast timing resolution.
- Prevent streamers and discharges that could damage the RPC.
- Ensure high efficiency in detecting charged particles.
- Provide a fast recovery time, allowing the RPC to operate at high rates.

4.4 Previous Experiments and Results

First Beam time at R³B:

RPC efficiency higher than 95 %. Good synchrony between RPC and the other detectors. Detector and DAQ were stable during the two weeks of beam time.

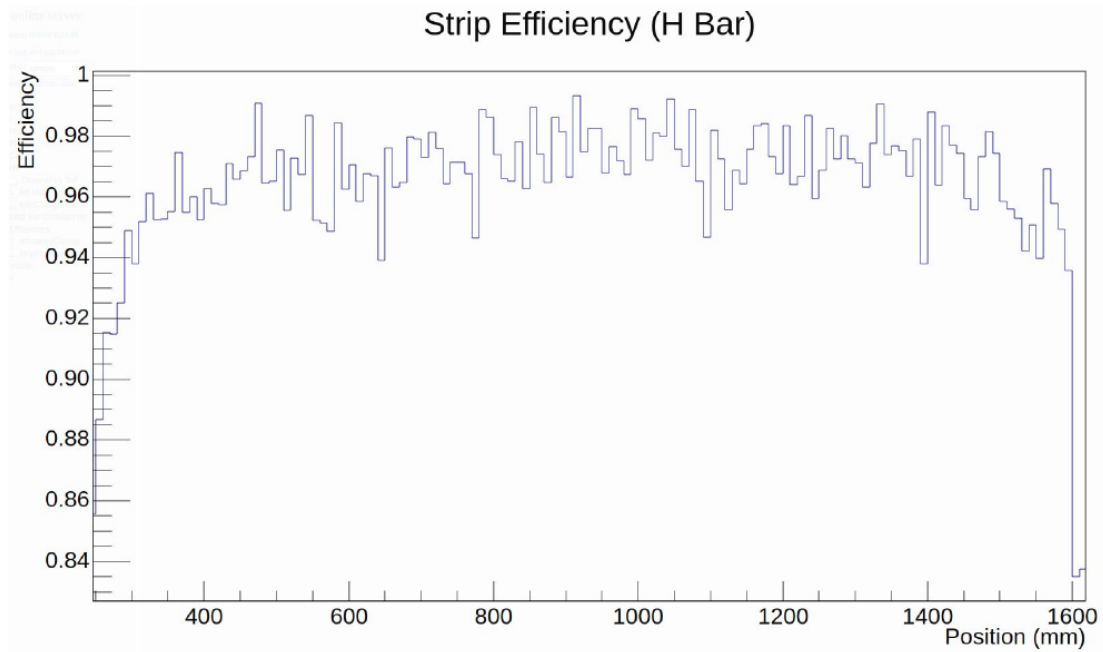


Figure 4.2: RPC Strip Efficiency

4.5 Preparation for an Experiment

Before each experiment Flash the RPC with SF_6 to dry out the interior. An alternative (SF_6 is expensive) is to use Nitrogen. One has to be careful with the pressure because if it's too high it can inflate the RPC and damage it. This process takes about a week.

When preparing to insert the gas mixture in the RPC, to check if there are no leaks, one opens the gas bottles with the mass controllers closed and then closes the bottles and checks if the pressure drops in the gas line.

Then insert the gas mixture, place one vertical NeuLAND bar on each side and calibrate in coincidence with cosmic rays. This enables us to adjust the voltage of the electrodes and find the working point of the RPC. This process takes about a week.

4.6 Calibration

SIMULATION FRAMEWORK

Whenever there is a problem, it usually lies between the chair and the monitor.

Simulations are a fundamental component of modern nuclear physics experiments, providing a virtual environment where experimental setups, detector responses, and physical processes can be modeled and tested prior to data acquisition. The simulation work for this thesis relies on three key software tools: Geant4, ROOT, and R3BRoot. Together, they form a comprehensive framework that enables the design, implementation, analysis, and validation of realistic nuclear experiments. The following subsections provide a brief overview of each tool and their respective roles in this work.

The simulation work in this thesis was conducted using the R3BRoot framework, the dedicated simulation and analysis environment developed for experiments within the R³B collaboration. While R3BRoot was the only framework used directly, it is built upon two widely used and powerful tools in nuclear and high-energy physics: Geant4 and ROOT. A brief overview of these tools is presented here to provide context for the capabilities offered by R3BRoot.

5.1 Geant4

Geant4 [49] is a C++ toolkit developed by CERN for simulating the passage of particles through matter. It provides detailed physics models and tracking capabilities that allow for realistic modeling of particle interactions, energy loss, multiple scattering, and nuclear processes. Within R3BRoot, Geant4 is responsible for handling the physical transport of particles through the simulated experimental setup, including interactions with detector materials, magnetic fields, and other components. This embedded use of Geant4 ensures that the simulations reflect the underlying physics of the experiment with high fidelity.

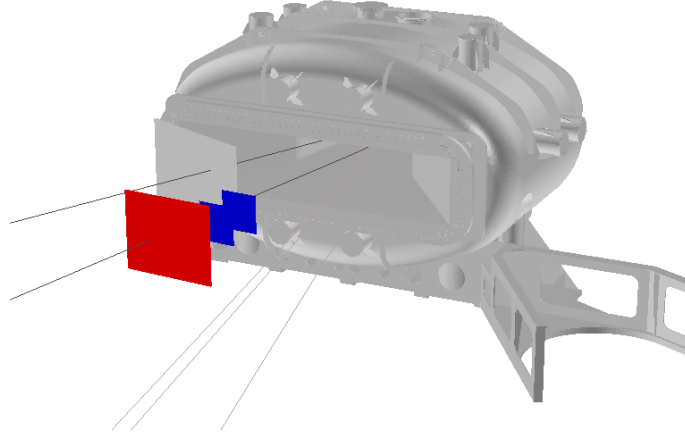


Figure 5.1: Example of an event in a simulation. In this case, there's a ^{14}C passing through ToFD, a Deuteron passing through the RPC and 3 neutrons going to NeuLAND.

5.2 ROOT

ROOT [50] is an object-oriented data analysis framework that provides tools for statistical analysis, histogramming, visualization, and data storage. R3BRoot integrates ROOT to manage event data, apply reconstruction algorithms, visualize results, and store output in ROOT-compatible formats. ROOT's capabilities are essential for handling the large volumes of simulated data produced and for performing the subsequent analysis and validation steps.

5.3 R3BRoot

R3BRoot [51] is the main framework used throughout this thesis for performing all simulation and analysis tasks. Developed specifically for experiments at the R³B setup, R3BRoot builds on the FairRoot framework and incorporates both Geant4 and ROOT. It provides pre-configured detector geometries, digitization routines, reconstruction algorithms, and analysis tools tailored to the R³B experimental environment.

Using R3BRoot, detailed simulations of the $^{25}\text{F}(p,2p)^{24}\text{O}$ experiment were performed, including particle generation, tracking through the GLAD magnet, propagation through the tracking detectors and the RPC, and emulation of detector responses. The framework also allowed the incorporation of realistic detector resolutions and systematics, enabling the generation of data that closely mirrors what will be observed experimentally. This simulated data formed the basis for developing and validating the Multidimensional Fitting functions presented in this thesis.

5.4 Plots

5.5 Multidimensional Fitting

In experiments like those conducted with the R^3B setup, the information directly recorded by detectors is often insufficient on its own to fully reconstruct the physical quantities of interest. Raw observables such as hit positions and times must be interpreted in the context of the particle's full trajectory, charge, and energy. To bridge this gap, multidimensional fitting (MDF) methods are used. These tools allow us to model complex, nonlinear relationships between measurable detector signals and the underlying physical properties of particles.

Multidimensional fitting is particularly powerful in the context of quasi-free scattering reactions, such as the one studied in the $^{25}\text{F}(p,2p)^{24}\text{O}$ experiment. Given the diversity and overlap of signals produced by different particles and trajectories in the R^3B setup, MDF enables a more accurate reconstruction of particle kinematics by using correlated detector data. It also allows us to compensate for the intrinsic limitations of individual detectors by combining information from multiple systems.

5.5.1 Application to the RPC and FOOT Detectors

In the simulation phase of this work, MDF techniques were employed to enhance the reconstruction of particle kinematics at the RPC detector — the main focus of this thesis. To train the fitting models, a realistic dataset was generated by simulating the propagation of particles expected to be detected in the experiment, namely protons, alpha particles, deuterons, and ^3He nuclei. These particles were tracked from their production near the target, through the downstream tracking detectors (FOOTs), the GLAD magnet, and finally to the RPC.

Nine input variables were selected to capture the relevant kinematic and spatial information of the particles:

1. The x, y, z positions at the first FOOT detector;
2. The directional angles of the particles (T_x and T_y), calculated from the positions at the first and second FOOTs;
3. The x, y, z positions at the RPC;
4. The time of flight between the last FOOT and the RPC.

These features encapsulate the spatial evolution and timing of the particle along its flight path, providing the necessary information to infer more abstract physical quantities.

Four distinct MDF functions were trained using this dataset:

- A function to estimate the momentum over charge (p/Q) of the particle;

- One function to estimate the momentum in x and another the momentum in y of the particle;
- A function to estimate the flight path (i.e., the actual distance traveled by the particle between the production point and the RPC).

Each function was trained separately to isolate specific aspects of the particle's motion and improve precision. These trained models can later be applied to experimental data to infer momentum and trajectory parameters with higher confidence than would be possible using analytic approximations alone.

This approach demonstrates the importance of data-driven tools like MDF in modern nuclear physics experiments, where complexity and high dimensionality make traditional reconstruction methods insufficient.

5.5.2 Validation of the MDF Models

Once the MDF models were trained, their performance was validated using a new set of Geant4 simulations that modeled a realistic experimental scenario. These simulations incorporated realistic beam-target reactions and included detector resolution effects, reproducing the uncertainties expected in the actual experiment.

For each simulated event, detector observables were extracted and fed into the trained MDF functions, which returned reconstructed values of the physical parameters. These were then compared against the known "true" values from the simulation. The difference between predicted and simulated values was analyzed through a series of performance plots.

The results demonstrated high predictive accuracy of the MDF functions. The residuals between predicted and true values were typically small, with uncertainties reaching down to the order of 10^{-3} in normalized units. This level of precision confirms that the trained functions are robust and reliable, making them suitable for application to real experimental data in the analysis phase.

The successful validation of these MDF models underscores their value as a reconstruction tool in complex experimental setups like R³B. They offer a data-driven approach to extracting meaningful physical insights from otherwise limited detector measurements, playing a central role in the broader simulation and analysis workflow of this thesis.

5.6 Conclusions for the Experiment

RESULTS

This is the results chapter
epigraph.

BIBLIOGRAPHY

- [1] E. Rutherford. "LXXIX. The scattering of α particles by matter and the structure of the atom". en. In: *The London, Edinburgh, and Dublin Philosophical Magazine and Journal of Science* 21.125 (1911-05), pp. 669–688. ISSN: 1941-5982, 1941-5990. DOI: [10.1080/14786440508637080](https://doi.org/10.1080/14786440508637080). URL: <https://www.tandfonline.com/doi/full/10.1080/14786440508637080> (cit. on p. 1).
- [2] C. F. von Weizsacker. "Zur Theorie der Kernmassen". de. In: *Eur. Phys. J. A* 96.7-8 (1935-07), pp. 431–458 (cit. on p. 2).
- [3] H. A. Bethe and R. F. Bacher. "Nuclear Physics A. Stationary States of Nuclei". en. In: *Reviews of Modern Physics* 8.2 (1936-04), pp. 82–229. ISSN: 0034-6861. DOI: [10.1103/RevModPhys.8.82](https://doi.org/10.1103/RevModPhys.8.82). URL: <https://link.aps.org/doi/10.1103/RevModPhys.8.82> (cit. on p. 2).
- [4] M. G. Mayer. "On Closed Shells in Nuclei". In: *Phys. Rev.* 74 (3 1948-08), pp. 235–239. DOI: [10.1103/PhysRev.74.235](https://doi.org/10.1103/PhysRev.74.235). URL: <https://link.aps.org/doi/10.1103/PhysRev.74.235> (cit. on p. 2).
- [5] O. Haxel and J. H. D. Jensen. "On the "Magic Numbers" in Nuclear Structure". en. In: () (cit. on pp. 2, 3).
- [6] M. G. Mayer and J. H. D. Jensen. *Elementary Theory of Nuclear Shell Structure*. Wiley, 1955 (cit. on p. 2).
- [7] W. M. Elsasser. "Sur le principe de Pauli dans les noyaux". fr. In: *Journal de Physique et le Radium* 4.10 (1933), pp. 549–556. ISSN: 0368-3842. DOI: [10.1051/jphysrad:01933004010054900](https://doi.org/10.1051/jphysrad:01933004010054900). URL: <http://www.edpsciences.org/10.1051/jphysrad:01933004010054900> (cit. on p. 2).
- [8] M. G. Mayer, J. Hans, and D. Jensen. "SHELL CLOSURE AND jj COUPLING". en. In: *Alpha-, Beta- and Gamma-Ray Spectroscopy*. Elsevier, 1968, pp. 557–582. ISBN: 978-0-7204-0083-0. DOI: [10.1016/B978-0-7204-0083-0.50020-1](https://doi.org/10.1016/B978-0-7204-0083-0.50020-1). URL: <https://linkinghub.elsevier.com/retrieve/pii/B9780720400830500201> (cit. on p. 2).

-
- [9] K. S. Krane. *Introductory nuclear physics*. en. Rev. ed., [Nachdr.] Hoboken, NJ: Wiley, 1988. ISBN: 978-0-471-80553-3 (cit. on p. 3).
- [10] T. Otsuka et al. “Evolution of shell structure in exotic nuclei”. en. In: *Reviews of Modern Physics* 92.1 (2020-03), p. 015002. ISSN: 0034-6861, 1539-0756. DOI: [10.1103/RevModPhys.92.015002](https://doi.org/10.1103/RevModPhys.92.015002). URL: <https://link.aps.org/doi/10.1103/RevModPhys.92.015002> (cit. on p. 4).
- [11] P. Spiller et al. “The FAIR Heavy Ion Synchrotron SIS100”. en. In: *Journal of Instrumentation* 15.12 (2020-12), T12013–T12013. ISSN: 1748-0221. DOI: [10.1088/1748-0221/15/12/T12013](https://doi.org/10.1088/1748-0221/15/12/T12013). URL: <https://iopscience.iop.org/article/10.1088/1748-0221/15/12/T12013> (cit. on p. 4).
- [12] M. Winkler et al. “The status of the Super-FRS in-flight facility at FAIR”. en. In: *Nuclear Instruments and Methods in Physics Research Section B: Beam Interactions with Materials and Atoms* 266.19-20 (2008-10), pp. 4183–4187. ISSN: 0168583X. DOI: [10.1016/j.nimb.2008.05.073](https://doi.org/10.1016/j.nimb.2008.05.073). URL: <https://linkinghub.elsevier.com/retrieve/pii/S0168583X080007015> (cit. on p. 4).
- [13] C. Sturm, B. Sharkov, and H. Stöcker. “1, 2, 3 ... FAIR !” en. In: *Nuclear Physics A* 834.1-4 (2010-03), pp. 682c–687c. ISSN: 03759474. DOI: [10.1016/j.nuclphysa.2010.01.124](https://doi.org/10.1016/j.nuclphysa.2010.01.124). URL: <https://linkinghub.elsevier.com/retrieve/pii/S0375947410001259> (cit. on p. 5).
- [14] G. Rosner. “Future Facility: FAIR at GSI”. en. In: *Nuclear Physics B - Proceedings Supplements* 167 (2007-05), pp. 77–81. ISSN: 09205632. DOI: [10.1016/j.nuclphysbps.2006.12.089](https://doi.org/10.1016/j.nuclphysbps.2006.12.089). URL: <https://linkinghub.elsevier.com/retrieve/pii/S0920563206010516> (cit. on p. 5).
- [15] H. Stoecker and C. Sturm. “The FAIR start”. en. In: *Nuclear Physics A* 855.1 (2011-04), pp. 506–509. ISSN: 03759474. DOI: [10.1016/j.nuclphysa.2011.02.117](https://doi.org/10.1016/j.nuclphysa.2011.02.117). URL: <https://linkinghub.elsevier.com/retrieve/pii/S0375947411002041> (cit. on p. 5).
- [16] T. Stöhlker et al. “APPA at FAIR: From fundamental to applied research”. en. In: *Nuclear Instruments and Methods in Physics Research Section B: Beam Interactions with Materials and Atoms* 365 (2015-12), pp. 680–685. ISSN: 0168583X. DOI: [10.1016/j.nimb.2015.07.077](https://doi.org/10.1016/j.nimb.2015.07.077). URL: <https://linkinghub.elsevier.com/retrieve/pii/S0168583X15006552> (cit. on p. 5).
- [17] K. Agarwal. “The Compressed Baryonic Matter (CBM) Experiment at FAIR – Physics, Status and Prospects”. en. In: *Physica Scripta* (2023-02). ISSN: 0031-8949, 1402-4896. DOI: [10.1088/1402-4896/acbca7](https://doi.org/10.1088/1402-4896/acbca7). URL: <https://iopscience.iop.org/article/10.1088/1402-4896/acbca7> (cit. on p. 5).

- [18] M. Destefanis. “The PANDA experiment at FAIR”. en. In: *Nuclear Physics B - Proceedings Supplements* 245 (2013-12), pp. 199–206. ISSN: 09205632. DOI: [10.1016/j.nuclphysbps.2013.10.040](https://doi.org/10.1016/j.nuclphysbps.2013.10.040). URL: <https://linkinghub.elsevier.com/retrieve/pii/S0920563213006269> (cit. on p. 5).
- [19] T. Nilsson and for the NUSTAR collaboration. “The NUSTAR project at FAIR”. en. In: *Physica Scripta* T166 (2015-11), p. 014070. ISSN: 0031-8949, 1402-4896. DOI: [10.1088/0031-8949/2015/T166/014070](https://doi.org/10.1088/0031-8949/2015/T166/014070). URL: <https://iopscience.iop.org/article/10.1088/0031-8949/2015/T166/014070> (cit. on p. 6).
- [20] G. R. Satchler. *Direct nuclear reactions*. 1983-01 (cit. on p. 8).
- [21] G. Jacob and T. A. J. Maris. “Quasi-Free Scattering and Nuclear Structure”. en. In: *Reviews of Modern Physics* 38.1 (1966-01), pp. 121–142. ISSN: 0034-6861. DOI: [10.1103/RevModPhys.38.121](https://doi.org/10.1103/RevModPhys.38.121). URL: <https://link.aps.org/doi/10.1103/RevModPhys.38.121> (cit. on p. 9).
- [22] G. Jacob and T. A. J. Maris. “Quasi-Free Scattering and Nuclear Structure. II.” en. In: *Reviews of Modern Physics* 45.1 (1973-01), pp. 6–21. ISSN: 0034-6861. DOI: [10.1103/RevModPhys.45.6](https://doi.org/10.1103/RevModPhys.45.6). URL: <https://link.aps.org/doi/10.1103/RevModPhys.45.6> (cit. on p. 9).
- [23] T. Aumann, C. A. Bertulani, and J. Ryckebusch. “Quasifree ($p, 2p$) and (p, pn) reactions with unstable nuclei”. en. In: *Physical Review C* 88.6 (2013-12), p. 064610. ISSN: 0556-2813, 1089-490X. DOI: [10.1103/PhysRevC.88.064610](https://doi.org/10.1103/PhysRevC.88.064610). URL: <https://link.aps.org/doi/10.1103/PhysRevC.88.064610> (cit. on p. 10).
- [24] V. Panin, T. Aumann, and C. A. Bertulani. “Quasi-free scattering in inverse kinematics as a tool to unveil the structure of nuclei: A tribute to Mahir S. Hussein”. en. In: *The European Physical Journal A* 57.3 (2021-03), p. 103. ISSN: 1434-6001, 1434-601X. DOI: [10.1140/epja/s10050-021-00416-9](https://doi.org/10.1140/epja/s10050-021-00416-9). URL: <https://link.springer.com/10.1140/epja/s10050-021-00416-9> (cit. on p. 10).
- [25] O. Hen et al. “Nucleon-nucleon correlations, short-lived excitations, and the quarks within”. en. In: *Reviews of Modern Physics* 89.4 (2017-11), p. 045002. ISSN: 0034-6861, 1539-0756. DOI: [10.1103/RevModPhys.89.045002](https://doi.org/10.1103/RevModPhys.89.045002). URL: <https://link.aps.org/doi/10.1103/RevModPhys.89.045002> (cit. on p. 10).
- [26] M. Duer et al. “Direct Observation of Proton-Neutron Short-Range Correlation Dominance in Heavy Nuclei”. en. In: *Physical Review Letters* 122.17 (2019-05), p. 172502. ISSN: 0031-9007, 1079-7114. DOI: [10.1103/PhysRevLett.122.172502](https://doi.org/10.1103/PhysRevLett.122.172502). URL: <https://link.aps.org/doi/10.1103/PhysRevLett.122.172502> (cit. on p. 10).
- [27] A. Schmidt et al. “Probing the core of the strong nuclear interaction”. en. In: *Nature* 578.7796 (2020-02), pp. 540–544. ISSN: 0028-0836, 1476-4687. DOI: [10.1038/s41586-020-2021-6](https://doi.org/10.1038/s41586-020-2021-6). URL: <https://www.nature.com/articles/s41586-020-2021-6> (cit. on p. 10).

- [28] F. M. Marqués et al. “Detection of neutron clusters”. en. In: *Physical Review C* 65.4 (2002-04), p. 044006. ISSN: 0556-2813, 1089-490X. DOI: [10.1103/PhysRevC.65.044006](https://doi.org/10.1103/PhysRevC.65.044006). URL: <https://link.aps.org/doi/10.1103/PhysRevC.65.044006> (cit. on p. 11).
- [29] F. M. Marqués and J. Carbonell. “The quest for light multineutron systems”. en. In: *The European Physical Journal A* 57.3 (2021-03), p. 105. ISSN: 1434-6001, 1434-601X. DOI: [10.1140/epja/s10050-021-00417-8](https://doi.org/10.1140/epja/s10050-021-00417-8). URL: <https://link.springer.com/10.1140/epja/s10050-021-00417-8> (cit. on p. 11).
- [30] M. Duer et al. “Observation of a correlated free four-neutron system”. en. In: *Nature* 606.7915 (2022-06), pp. 678–682. ISSN: 0028-0836, 1476-4687. DOI: [10.1038/s41586-022-04827-6](https://doi.org/10.1038/s41586-022-04827-6). URL: <https://www.nature.com/articles/s41586-022-04827-6> (cit. on p. 11).
- [31] V. Panin et al. “Unveiling the structure of neutron-rich $Z=9$ isotopes: the case of ^{25}F ”. Unpublished research proposal submitted to GSI Helmholtzzentrum für Schwerionenforschung. 2024 (cit. on pp. 12, 17, 19, 22).
- [32] D. S. Ahn et al. “Location of the Neutron Dripline at Fluorine and Neon”. en. In: *Physical Review Letters* 123.21 (2019-11), p. 212501. ISSN: 0031-9007, 1079-7114. DOI: [10.1103/PhysRevLett.123.212501](https://doi.org/10.1103/PhysRevLett.123.212501). URL: <https://link.aps.org/doi/10.1103/PhysRevLett.123.212501> (cit. on p. 12).
- [33] V. Panin et al. “Exclusive measurements of quasi-free proton scattering reactions in inverse and complete kinematics”. en. In: *Physics Letters B* 753 (2016-02), pp. 204–210. ISSN: 03702693. DOI: [10.1016/j.physletb.2015.11.082](https://doi.org/10.1016/j.physletb.2015.11.082). URL: <https://linkinghub.elsevier.com/retrieve/pii/S0370269315009612> (cit. on p. 12).
- [34] K. Boretzky et al. “NeuLAND: The high-resolution neutron time-of-flight spectrometer for R3B at FAIR”. en. In: *Nuclear Instruments and Methods in Physics Research Section A: Accelerators, Spectrometers, Detectors and Associated Equipment* 1014 (2021-10), p. 165701. ISSN: 01689002. DOI: [10.1016/j.nima.2021.165701](https://doi.org/10.1016/j.nima.2021.165701). URL: <https://linkinghub.elsevier.com/retrieve/pii/S0168900221006860> (cit. on pp. 12, 23).
- [35] A. O. Macchiavelli et al. “Core of F^{25} in the rotational model”. en. In: *Physical Review C* 102.4 (2020-10), p. 041301. ISSN: 2469-9985, 2469-9993. DOI: [10.1103/PhysRevC.102.041301](https://doi.org/10.1103/PhysRevC.102.041301). URL: <https://link.aps.org/doi/10.1103/PhysRevC.102.041301> (cit. on p. 12).
- [36] GSI Helmholtzzentrum für Schwerionenforschung GmbH. *Accelerator Facility* — [gsi.de](https://www.gsi.de/en/researchaccelerators/accelerator_facility). https://www.gsi.de/en/researchaccelerators/accelerator_facility. [Accessed 16-05-2025] (cit. on p. 13).

- [37] R. Hollinger et al. "Status of high current ion source operation at the GSI accelerator facility". en. In: *Review of Scientific Instruments* 79.2 (2008-02), p. 02C703. ISSN: 0034-6748, 1089-7623. DOI: [10.1063/1.2801623](https://doi.org/10.1063/1.2801623). URL: <https://pubs.aip.org/rsi/article/79/2/02C703/1068369/Status-of-high-current-ion-source-operation-at-the> (cit. on p. 14).
- [38] H. Vormann et al. "High current heavy ion beam investigations at GSI-UNILAC". en. In: *Journal of Physics: Conference Series* 2420.1 (2023-01), p. 012037. ISSN: 1742-6588, 1742-6596. DOI: [10.1088/1742-6596/2420/1/012037](https://doi.org/10.1088/1742-6596/2420/1/012037). URL: <https://iopscience.iop.org/article/10.1088/1742-6596/2420/1/012037> (cit. on p. 14).
- [39] W. Barth et al. "High brilliance beam investigations at the universal linear accelerator". en. In: *Physical Review Accelerators and Beams* 25.4 (2022-04), p. 040101. ISSN: 2469-9888. DOI: [10.1103/PhysRevAccelBeams.25.040101](https://doi.org/10.1103/PhysRevAccelBeams.25.040101). URL: <https://link.aps.org/doi/10.1103/PhysRevAccelBeams.25.040101> (cit. on p. 14).
- [40] R. Singh. "Tune measurement at GSI SIS-18: Methods and applications". In: (2014) (cit. on p. 14).
- [41] GSI Helmholtzzentrum für Schwerionenforschung GmbH. *SIS18 Sections* — [gsi.de. https://www.gsi.de/en/work/accelerator_operations/accelerators/heavy_ion_synchrotron_sis18/sis18_sections](https://www.gsi.de/en/work/accelerator_operations/accelerators/heavy_ion_synchrotron_sis18/sis18_sections). [Accessed 16-05-2025] (cit. on p. 15).
- [42] H. Geissel and Y. A. Litvinov. "Experiments with the FRS facility at GSI". en. In: *Nuclear Instruments and Methods in Physics Research Section B: Beam Interactions with Materials and Atoms* 266.19-20 (2008-10), pp. 4176–4182. ISSN: 0168583X. DOI: [10.1016/j.nimb.2008.05.093](https://doi.org/10.1016/j.nimb.2008.05.093). URL: <https://linkinghub.elsevier.com/retrieve/pii/S0168583X08007003> (cit. on p. 15).
- [43] GSI Helmholtzzentrum für Schwerionenforschung GmbH. *WebHome & FRS & GSI Wiki* — [wiki.gsi.de. https://wiki.gsi.de/FRS/](https://wiki.gsi.de/FRS/). [Accessed 16-05-2025] (cit. on p. 16).
- [44] M. Mager. "ALPIDE, the Monolithic Active Pixel Sensor for the ALICE ITS upgrade". en. In: *Nuclear Instruments and Methods in Physics Research Section A: Accelerators, Spectrometers, Detectors and Associated Equipment* 824 (2016-07), pp. 434–438. ISSN: 01689002. DOI: [10.1016/j.nima.2015.09.057](https://doi.org/10.1016/j.nima.2015.09.057). URL: <https://linkinghub.elsevier.com/retrieve/pii/S0168900215011122> (cit. on p. 21).
- [45] S. Paschalis et al. "The in-beam tracking detectors of the R³B experiment". en. In: (2015). Medium: Abstract Publisher: GSI Helmholtzzentrum fuer Schwerionenforschung, Darmstadt. DOI: [10.15120/GR-2015-1-MU-NUSTAR-NR-15](https://doi.org/10.15120/GR-2015-1-MU-NUSTAR-NR-15). URL: <https://repository.gsi.de/record/183947> (cit. on p. 21).
- [46] D. Cortina-Gil et al. "CALIFA, a Dedicated Calorimeter for the R3B/FAIR". en. In: *Nuclear Data Sheets* 120 (2014-06), pp. 99–101. ISSN: 00903752. DOI: [10.1016/j.nds.2014.07.017](https://doi.org/10.1016/j.nds.2014.07.017). URL: <https://linkinghub.elsevier.com/retrieve/pii/S0090375214004694> (cit. on p. 22).

- [47] M. Heil et al. “A new Time-of-flight detector for the R³B setup”. en. In: *The European Physical Journal A* 58.12 (2022-12), p. 248. ISSN: 1434-601X. DOI: [10.1140/epja/s10050-022-00875-8](https://doi.org/10.1140/epja/s10050-022-00875-8). URL: <https://link.springer.com/10.1140/epja/s10050-022-00875-8> (cit. on p. 23).
- [48] M. Xarepe et al. “Resistive plate chambers for precise measurement of high-momentum protons in short range correlations at R³B”. en. In: *Nuclear Instruments and Methods in Physics Research Section A: Accelerators, Spectrometers, Detectors and Associated Equipment* 1055 (2023-10), p. 168445. ISSN: 01689002. DOI: [10.1016/j.nima.2023.168445](https://doi.org/10.1016/j.nima.2023.168445). URL: <https://linkinghub.elsevier.com/retrieve/pii/S0168900223004357> (cit. on p. 23).
- [49] S. Agostinelli et al. “Geant4—a simulation toolkit”. en. In: *Nuclear Instruments and Methods in Physics Research Section A: Accelerators, Spectrometers, Detectors and Associated Equipment* 506.3 (2003-07), pp. 250–303. ISSN: 01689002. DOI: [10.1016/S0168-9002\(03\)01368-8](https://doi.org/10.1016/S0168-9002(03)01368-8). URL: <https://linkinghub.elsevier.com/retrieve/pii/S0168900203013688> (cit. on p. 31).
- [50] R. Brun and F. Rademakers. “ROOT — An object oriented data analysis framework”. en. In: *Nuclear Instruments and Methods in Physics Research Section A: Accelerators, Spectrometers, Detectors and Associated Equipment* 389.1-2 (1997-04), pp. 81–86. ISSN: 01689002. DOI: [10.1016/S0168-9002\(97\)00048-X](https://doi.org/10.1016/S0168-9002(97)00048-X). URL: <https://linkinghub.elsevier.com/retrieve/pii/S016890029700048X> (cit. on p. 32).
- [51] D. Bertini. “R3BRoot, simulation and analysis framework for the R³B experiment at FAIR”. en. In: *Journal of Physics: Conference Series* 331.3 (2011-12), p. 032036. ISSN: 1742-6596. DOI: [10.1088/1742-6596/331/3/032036](https://doi.org/10.1088/1742-6596/331/3/032036). URL: <https://iopscience.iop.org/article/10.1088/1742-6596/331/3/032036> (cit. on p. 32).

A

RPC PLOTS

GSI ACCELERATOR FACILITY

